CELL BIOLOGY

Nanoscale coupling of endocytic pit growth and stability

Martin Lehmann¹*, Ilya Lukonin^{1†}, Frank Noé^{2,3}, Jan Schmoranzer⁴, Cecilia Clementi^{2,3}, Dinah Loerke⁵, Volker Haucke^{1,6}*

Clathrin-mediated endocytosis, an essential process for plasma membrane homeostasis and cell signaling, is characterized by stunning heterogeneity in the size and lifetime of clathrin-coated endocytic pits (CCPs). If and how CCP growth and lifetime are coupled and how this relates to their physiological function are unknown. We combine computational modeling, automated tracking of CCP dynamics, electron microscopy, and functional rescue experiments to demonstrate that CCP growth and lifetime are closely correlated and mechanistically linked by the early-acting endocytic F-BAR protein FCHo2. FCHo2 assembles at the rim of CCPs to control CCP growth and lifetime by coupling the invagination of early endocytic intermediates to clathrin lattice assembly. Our data suggest a mechanism for the nanoscale control of CCP growth and stability that may similarly apply to other metastable structures in cells.

Copyright © 2019
The Authors, some rights reserved; exclusive licensee
American Association for the Advancement of Science. No claim to original U.S. Government Works. Distributed under a Creative
Commons Attribution
NonCommercial
License 4.0 (CC BY-NC).

INTRODUCTION

Clathrin-mediated endocytosis (CME) is an essential cell physiological process that dynamically controls the composition of the plasma membrane and thereby regulates a plethora of functions ranging from nutrient uptake and cell signaling to the formation of morphogen gradients and synaptic transmission (1-3). CME is initiated by the adaptor-mediated assembly of metastable clathrin-coated pits (CCPs) that dynamically exchange their components with soluble endocytic proteins. Metastability, indeed, is a characteristic hallmark of endocytic vesicle formation (4) and other dynamic cellular processes. CCP assembly is accompanied or followed by the progressive invagination of the membrane, eventually leading to the dynamin-dependent scission of a clathrin-coated vesicle (CCV) that delivers its cargo to the endosomal system (1, 2). In addition to metastable CCPs, mammalian cells also harbor flat hexagonal clathrin lattices that represent stable platforms (i.e., with lifetimes of >10 min) for plasma membrane organization (5, 6) distinct from endocytic carriers (i.e., CCPs and CCVs).

Endocytic CCPs display a wide heterogeneity in size and lifetime within cells that ranges from less than 20 s to a few minutes (7-10). Moreover, CCP lifetimes vary between cell types and during development (9). Short-lived CCPs (>20 s) comprise unstable abortive intermediates that fail to progress along the pathway of productive endocytic vesicle formation (7, 11, 12). CCP lifetimes thus can be considered a reflection of their stability. If and how the lifetime distribution of CCPs and, therefore, their stability are related to CCP growth are unknown. According to a simple avidity-based model of CME (4), the lifetime and stability of forming CCPs may be determined by the number of clathrin molecules and associated

early-acting endocytic proteins accumulated during the onset of CME given that the number of possible interactions in a multivalent protein interaction network increases nonlinearly with the number of endocytic proteins (13). This hypothesis is consistent with recent findings suggesting that membrane bending, a decisive step in determining whether a productive vesicle is formed, occurs preferentially once the majority of the final clathrin content has been acquired (14–17) [although some CCPs may start to bend immediately (16)]. In the present study, we combine computational modeling with automated tracking of CCP dynamics and electron microscopy (EM) to show that endocytic CCP growth and stability are coupled on the nanoscale by an early-acting endocytic protein.

RESULTS

Endocytic protein content and CCP lifetime are correlated

We developed a computational model (described in Materials and Methods) that simulates the association and assembly of clathrin at the membrane in a two-dimensional (2D) lattice, i.e., in the absence of curvature generation and fission. The model describes the binding, dissociation, and self-assembly of clathrin in the presence of its major adaptor complex AP2 and the extended FCH homology Bin-Amphiphysin-Rvs (F-BAR) domain (18, 19) protein FCHo2, which has been postulated to either nucleate (20) or stabilize CCPs (8, 21, 22) at an early stage, in part, by facilitating AP2 activation (23). Simulating the size of clathrin structures over time revealed the formation of extended clathrin lattices that remained stable for the remainder of the simulation (Fig. 1, A and B), suggesting that the formation of sufficiently large and stable clathrin assemblies may be a critical step in the assembly of productive endocytic CCPs. These observations from simulation experiments are most consistent with a model according to which endocytic protein (e.g., clathrin or FCHo2) content and CCP lifetime are correlated. We tested this hypothesis by quantitative dual-color total internal reflection fluorescence (TIRF) microscopy analysis of CCP dynamics in living cells (i.e., cell lines that are largely devoid of stable flat clathrin lattices). To this aim, we modified a previously established algorithm for the automated detection, filtering, and quantification of the dynamics of thousands of CCPs from live TIRF imaging of HeLa or

¹Leibniz-Forschungsinstitut für Molekulare Pharmakologie (FMP), 13125 Berlin, Germany. ²Freie Universität Berlin, Department of Mathematics and Computer Science and Department of Physics, 14195 Berlin, Germany. ³Center for Theoretical Biological Physics and Department of Chemistry, Rice University, Houston, TX 77005, USA. ⁴Charité Universitätsmedizin Berlin, Virchowweg 6, 10117 Berlin, Germany. ⁵Department of Physics and Astronomy, University of Denver, Denver, CO 80208, USA. ⁶Freie Universität Berlin, Faculty of Biology, Chemistry, Pharmacy, 14195 Berlin, Germany. *Corresponding author. Email: haucke@fmp-berlin.de (V.H.); mlehmann@fmp-berlin.de (M.L.)

[†]Present address: Friedrich Miescher Institute for Biomedical Research (FMI), Maulbeerstrasse 66, 4058 Basel, Switzerland.

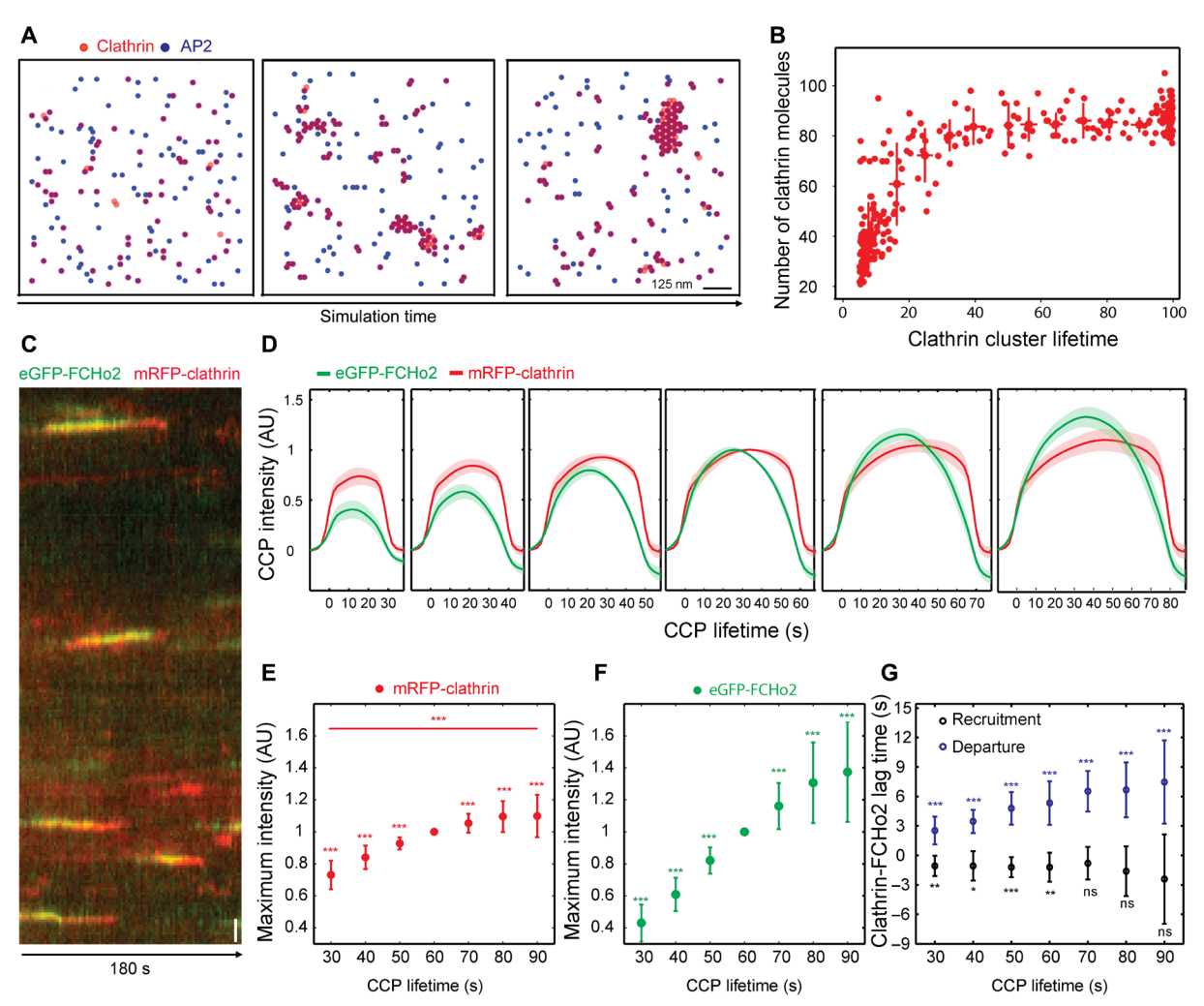


Fig. 1. Coupling of CCP growth and stability via the early-acting endocytic FBAR domain protein FCHo2. (A) Snapshots of clathrin clusters observed in simulations over time in the presence of 180 clathrin, 180 AP2, and 50 FCHo2 molecules. (B) Number of clathrin molecules per cluster as a function of cluster lifetime. The lifetime is measured in units of 10^6 simulation time steps. (C) Example kymograph derived from dual-color TIRF microscopy analysis of HeLa cells coexpressing eGFP-FCHo2 and mRFP-clathrin light chain. Scale bar, $1 \mu m$. (D to F) Early endocytic protein content and CCP lifetime are correlated. (D) Normalized maximum intensity of clathrin (red) and FCHo2 (green) for different lifetime cohorts as mean intensity (solid line) and SD (shaded area). CCP lifetime closely correlates with clathrin and FCHo2 intensity. (E) Clathrin content and CCP lifetime are correlated. Normalized mean intensity of mRFP-clathrin for different lifetime cohorts (30, 40, 50, 60, 70, and 80 s) from n = 15 cells with >1500 trajectories per cell. (F) FCHo2 content and CCP lifetime are correlated with FCHo2 being recruited preferentially to long-lived CCPs. Normalized mean intensity of eGFP-FCHo2 for different lifetime cohorts (30, 40, 50, 60, 70, and 80 s) from n = 15 cells with >1500 trajectories per cell. (G) FCHo2 is correcruited with clathrin to CCPs but dissociates prior to clathrin. Lag times between clathrin and FCHo2 were calculated from half-maximum intensity time points of each color (clathrin-FCHo2) for the CCP initiation phase (black) or the CCP departure phase (blue). Means \pm SD from the same data set as in (D). One-sided t test, t test,

Cos7 cells expressing monomeric red fluorescent protein (mRFP)—tagged clathrin light chain (see Materials and Methods). We devised an automated detection and analysis scheme that allowed us to quantitatively analyze CCP lifetime from thousands of individual authentic endocytic events (fig. S1) (11) characterized by low lateral mobility (e.g., to avoid detection of en passant clathrin-positive endosomes or other short-lived motile clathrin structures of unclear origin). The cumulative lifetime distribution of these authentic CCPs followed a single exponential function with a time constant λ of about 70 s and a high overall variability that ranged from 20 up to about 180 s, consistent with recent data from genome-engineered cells (7, 10), which show that authentic CME sites display comparably long lifetimes (11). We then asked whether the lifetimes of CCPs were cor-

related with clathrin protein content, which is directly proportional to CCP size (1). Short-lived CCPs with lifetimes of 30 to 40 s contained a significantly lower number of clathrin molecules than CCPs with lifetimes of 70 s or more (Fig. 1, C to E), suggesting that CCP lifetime and growth are correlated by a, so far, unknown mechanism. It has been shown that much of the variability in the lifetime of CCPs is due to early events that lead to the assembly of about 70% or more of the final clathrin content, while the late phases of CCP invagination and fission occur with relatively constant timing (16). On the basis of these data and our results from simulation experiments, we reasoned that the growth and, therefore, the lifetime of CCPs are likely to be determined by early-acting factors such as FCHo2. When we analyzed the lifetime distribution and FCHo2 protein content by dual-color

TIRF microscopy combined with automated particle tracking, we indeed observed a notable enrichment of green fluorescent protein (GFP)–FCHo2 in long-lived CCPs, while short-lived CCPs were deprived of FCHo2 relative to clathrin (Fig. 1D). Similar results were seen for mCherry-FCHo2 imaged together with GFP-clathrin (fig. S2, A and B). When FCHo2 content and CCP lifetime were plotted, a near-linear relationship emerged (Fig. 1F). These data indicate that the lifetime of CCPs is correlated with FCHo2 and clathrin protein content and, hence, with CCP growth. Short-lived CCPs often are nonproductive; therefore, CCP lifetime and growth likely control the efficacy of CME (see below).

How CCPs are nucleated and grow initially and what the role of FCHo proteins might be remain debated. The close correlation between CCP lifetime and FCHo2 content suggests that FCHo2 may act at an early stage of CME to couple CCP growth and stability, e.g., by activating AP2 (23). In line with this hypothesis, we found that the timing of FCHo2 recruitment closely (within 1 to 2 s) matched the arrival of clathrin, but FCHo2 dissociated from mature CCPs significantly prior to clathrin (Fig. 1G and fig. S2C), possibly reflecting its propensity to associate with and stabilize low-curvature but not high-curvature membranes (24) characteristic of late-stage CCPs prior to scission (1, 2, 25, 26).

FCHo2 couples CCP growth and stability

These data prompted us to probe a possible function of FCHo2 in coupling CCP growth and stability by computational modeling. When the FCHo2 protein copy number was reduced 10-fold (akin to FCHo2 knockdown, see below), simulated clathrin structures remained much smaller in size and became unstable (Fig. 2, A and B), suggesting that the growth and lifetime of endocytic clathrin assemblies may be coupled via the clathrin/AP2-activating function of FCHo. We tested this model experimentally using a lentiviral system to quantitatively deplete FCHo proteins from cells. This system that is based on the selection of virus-infected puromycinresistant cells bears the advantage over knockout approaches that genetic compensation or clonal heterogeneities are unlikely to occur while achieving depletion of the target protein with an efficacy far superior to conventional knockdown approaches. We focused on the phenotypes caused by the loss of FCHo2 (Fig. 2C) as FCHo2 is the only FCHo isoform required for CME in Cos7 fibroblasts (compare Fig. 3, A and C) and in other cell types tested [i.e., HeLa and human embryonic kidney (HEK) 293T; fig. S3]. If FCHo2 content determines CCP growth and, thereby, lifetime, then loss of FCHo2 would be expected to shorten CCP lifetime and reduce CCP growth and stability. mRFP-clathrin-labeled CCPs in Cos7 cells devoid of FCHo2 appeared much dimmer in intensity, and many events were short-lived (Fig. 2D). Quantitative analyses by automated detection and tracking revealed a marked shift in the cumulative lifetime distribution of CCPs (Fig. 2E) that could be exponentially fit with a time constant of about 20 to 30 s in Cos7 cells lacking FCHo2 compared with 70 to 80 s in controls (Fig. 2F). Moreover, the average clathrin content of CCPs was reduced in FCHo2-depleted cells (Fig. 2H), indicating that shortening of CCP lifetime in the absence of FCHo2 correlates with and is likely caused by reduced CCP growth. These changes were not due to defective CCP initiation in the absence of FCHo2 (Fig. 2G), in contrast to earlier proposals (20).

To determine how defects in CCP growth and dynamics relate to the morphology of CCPs, we subjected FCHo2-depleted cells to morphometric ultrastructural analyses by EM. Both Cos7 and HEK293 cells lacking FCHo2 expression displayed a 30 to 50% reduction in the number of morphologically discernable CCPs (Fig. 2I). When clathrin-containing endocytic intermediates were grouped into different stages from early shallow to constricted CCPs and, lastly, to free CCVs, we found that lack of FCHo2 severely reduced the number of early shallow intermediates, resulting in a near twofold reduction in the number of productive CCVs formed (Fig. 2J). Moreover, quantitative EM reconstruction analysis of the shallow CCP profiles formed in Cos7 cells revealed significant reductions in the invagination depth (Fig. 2K) and size [nonsilencing shRNA (shNS), 332 ± 84 nm (mean ± SD); shFCHo2, 270 \pm 54 nm; t test, P = 0.00012] of early endocytic intermediates. The remaining CCVs that eventually managed to undergo successful assembly and scission even in the absence of FCHo2 were morphologically indistinguishable from those observed in control cells (fig. S4). These CCVs likely originate from the scission of the remaining productive CCPs that succeed to grow beyond the threshold required for CCP invagination (14, 15) and scission under conditions of FCHo2 loss.

Collectively, the results described indicate a close coupling of CCP growth (and, thus, CCP size) and lifetime in eukaryotic cells that requires the activity of the F-BAR protein FCHo2, which stabilizes early-stage CCPs and promotes their invagination. Failure of CCP growth and marked shortening of CCP lifetime are predicted to affect the efficacy of CME. Consistently, Cos7 fibroblasts lacking FCHo2 (Fig. 3A) displayed a prominent reduction, although not a complete block in transferrin (Tf)–CME (Fig. 3, B and C, and fig. S3C for HeLa and HEK293T cells) that scaled with the reduced numbers of CCPs and productive CCVs formed in FCHo2-depleted cells (compare Fig. 2, I and K). Loss of FCHo1 did not affect CME (Fig. 3, A to C and fig. S3 for HeLa and HEK293T cells), indicating that FCHo1 and FCHo2 are not functionally redundant, a conclusion further corroborated below.

FCHo2 controls CCP growth and stability via phosphoinositide binding and the shape of its F-BAR domain

To obtain insights into the mechanism by which FCHo2 couples CCP growth and lifetime in CME, we analyzed the nanoscale localization of FCHo2 at CCPs. Dual-color SD-dSTORM (spectral demixing direct stochastic optical reconstruction microscopy) analysis of the distribution of endogenous FCHo2 within CCPs followed by quantitative averaging of >250 images revealed a marked concentration of FCHo2 in ring-like structures (about 225 nm in diameter) at the outer rim of CCPs [consistent with (27)] while being largely absent from the CCP center (Fig. 3, D and E) that eventually gives rise to the dome as CCPs invaginate. Hence, FCHo2 selectively accumulates at the rim of CCPs, consistent with its early role in coupling CCP growth and dynamics.

Different models have been proposed regarding the early endocytic function of FCHo2. According to one model, FCHo2 nucleates CCPs by acting as a plasma membrane–associated recruitment hub for early-acting endocytic proteins bound to its μ -homology domain (20). This model predicts crucial roles for FCHo2's membrane-deforming F-BAR and C-terminal μ -homology domains in CME. Alternatively, the *Caenorhabditis elegans* ortholog of FCHo2 has been proposed to stabilize CCPs via a short peptide segment comprising the AP2 activating (APA) domain that allosterically switches the clathrin adaptor AP2 into its active conformation, thereby triggering clathrin assembly (23), while its F-BAR and μ -homology domains are dispensable for FCHo function. In principle, either of these models is compatible with the observed crucial role of

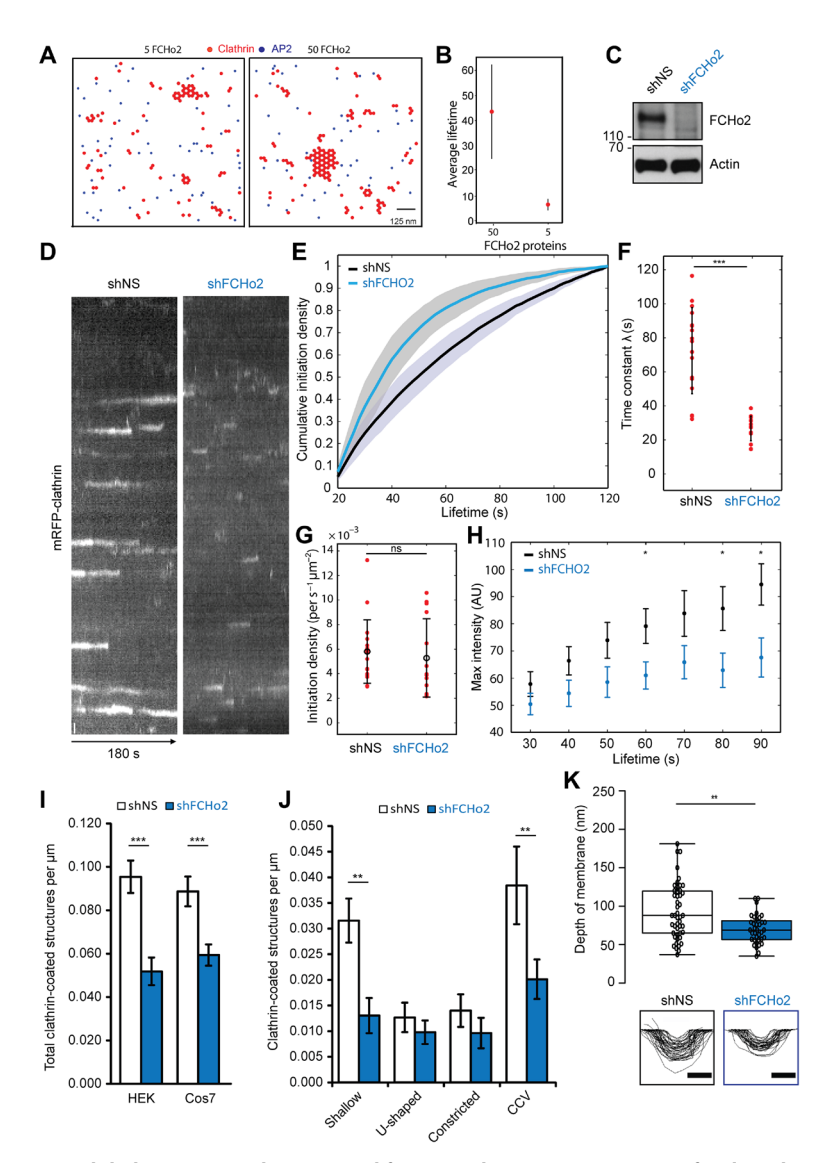


Fig. 2. Loss of FCHo2 reduces CCP size and clathrin content, shortens CCP lifetime, and impairs invagination of early endocytic intermediates. (A) Snapshots of clathrin clusters observed in simulations over time in the presence of 180 clathrin, 180 AP2, and either 5 (left) or 50 (right) FCHo2 molecules. (B) Average lifetime of clathrin clusters observed in simulations in the presence of 50 or 5 FCHo2 molecules. The lifetime is measured in units of 10⁶ simulation time steps. (C) Loss of FCHo2 protein expression by lentiviral knockdown. Immunoblot analysis of puromycin-selected Cos7 cells transduced with lentiviruses expressing nonsilencing control shRNA (shNS) or shRNAs targeting FCHo2 (shFCHo2). Actin was analyzed as a control protein. (D) Example kymograph derived from TIRF microscopy analysis of lentivirally transduced puromycin-selected Cos7 cells expressing mRFP-clathrin light chain (CLC). Left: shNS-expressing control cells. Right: shFCHo2-expressing cells. Scale bar, 1 µm. (E and F) Loss of FCHo2 shortens CCP lifetime. (E) Mean cumulative lifetime distribution for all cells (means ± SD in shaded area). Cumulative lifetime distribution is measured in each cell as a function of CCP lifetime, normalized to the value for the 60-s lifetime bin, and subsequently averaged between cells (shNS, n = 17 cells; shFCHo2, n = 14 cells; both from three independent experiments). (F) Distribution of time constants λ of exponential fits to the cumulative lifetime functions. Data from three independent experiments (with shNS n = 17 cells, shFCHo2 n = 14 cells) are shown, where $\lambda = 72 \pm 25$ s for shNS and $\lambda = 27 \pm 7$ s for shFCho2. (G) FCHo2 is dispensable for CCP nucleation. Total CCP initiation density including CCPs of the full range of lifetimes within the constrained population is found to be nonsignificantly different between control (shNS) and FCHo2-depleted Cos7 cells (P = 0.6142, t test of shFCHo2 versus shNS). (H) Loss of FCHo2 reduces the clathrin content of CCPs. Maximal clathrin intensity of CCP trajectories as function of trajectories' total lifetimes for shNS (black, n = 17 cells from three independent experiments) and shFCHo2 (blue, n = 14 cells from three independent experiments). Two-sided t test, *P ≤ 0.05. (I) FCHo2 loss reduces CCP density. Quantitative EM analysis of clathrin-coated endocytic intermediates in control (shNS) and FCHo2-depleted (shFCHo2) HEK293T and Cos7 cells. Bar diagram detailing the total density of clathrin-coated endocytic structures per micrometer cell perimeter. Cos7 cells: n = 3 experiments with a total of 42 cell profiles analyzed for shNS and shFcho2. HEK293T: n = 2 experiments with a total of 35 (shNS) and 36 cell profiles analyzed (shFcho2). Means ± SEM. (J) FCHo2 loss reduces the number of shallow early endocytic intermediates and free CCVs. Quantitative EM analysis of clathrin-coated endocytic intermediates in control (shNS) and FCHo2-depleted (shFCHo2) cells. Morphological groups were shallow, nonconstricted U-shaped, constricted Ω -shaped pits, or structures containing complete clathrin coats (CCVs). Bar diagram detailing the abundance of different CCS per micrometer cell perimeter. Analysis of 35 (shNS) and 36 cell profiles (shFcho2) depicted as means ± SEM. (K) Defective invagination and reduced size of early-stage endocytic intermediates in FCHo2-depleted cells. Analysis of the depth of clathrin-coated shallow early-stage endocytic intermediates in control (shNS) or FCHo2-depleted (shFCHo2) cells. A total of 27 and 31 cell profiles from two experiments were analyzed. Box plot shows the mean with 25th and 75th percentiles, and error bars represent minimum and maximum. Student's t test, (F to K): *** $P \le 0.001$, ** $P \le 0.01$, ** $P \le 0.05$.

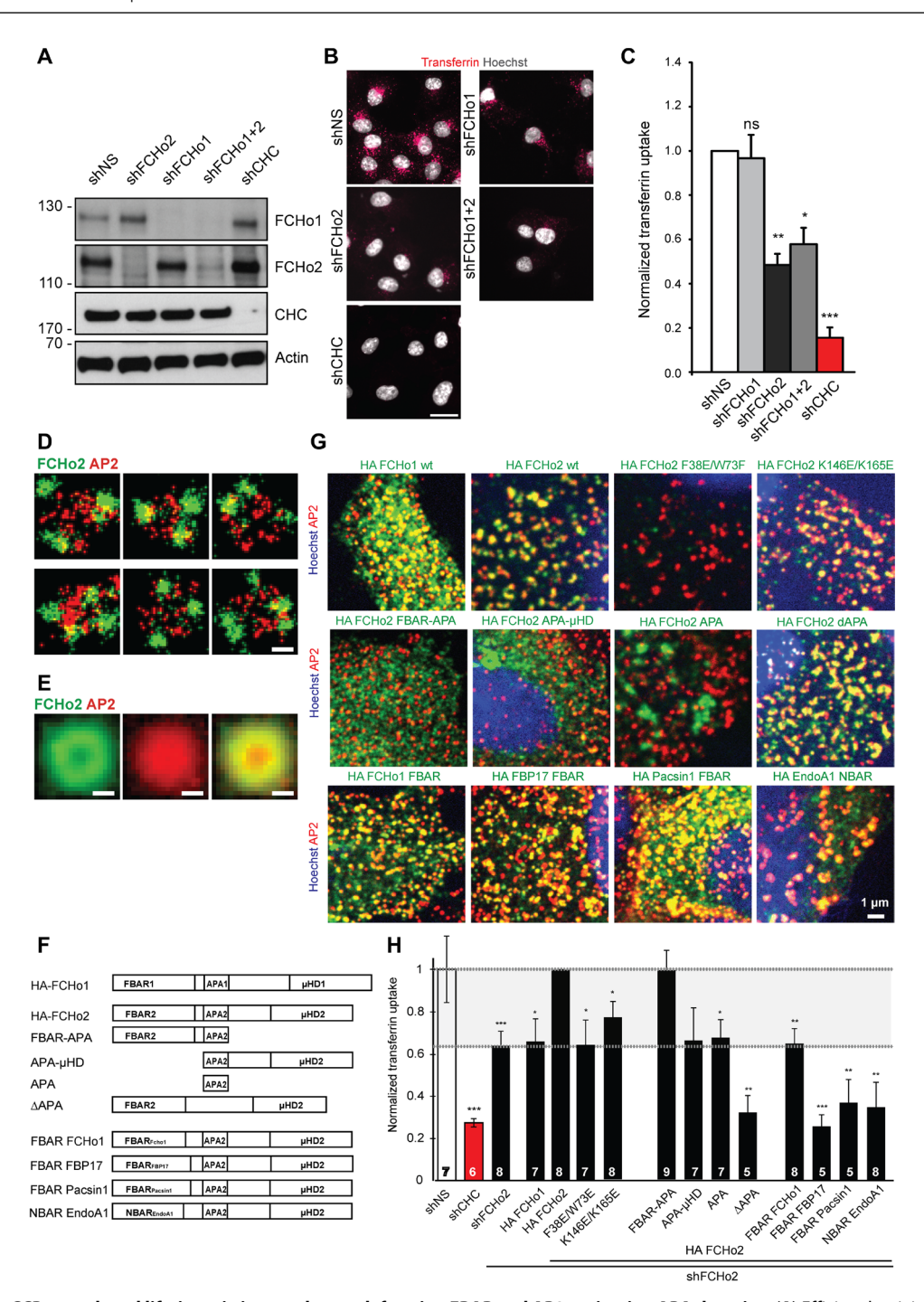


Fig. 3. FCHo2 couples CCP growth and lifetime via its membrane-deforming FBAR and AP2-activating APA domains. (A) Efficient lentiviral depletion of FCHo1, FCHo2, or clathrin heavy chain (CHC) from Cos7 cells. Immunoblot analysis of Cos7 cells transduced with lentiviruses expressing nonsilencing control shRNA (shNS) or shRNAs targeting FCHo1 (shFCHo1), FCHo2 (shFCHo2), or clathrin heavy chain (shCHC). Actin was analyzed as a loading control. (B) Representative images of Tf-CME in Cos7 cells transduced with lentiviruses as in (A). Scale bar, 10 μm. (C) Loss of FCHo2 impairs CME. Quantification of representative data shown in (A). One-sample t test, *** $P \le 0.01$, * $P \le 0.05$. (D) FCHo2 assembles at the rim of CCPs. Representative dual-color SD-dSTORM images of CCPs in methanol-fixed HeLa cells stained for endogenous FCHo2 (green) and AP2 (red). Scale bar, 100 nm. (E) FCHo2 assembles at the rim of CCPs. Averaged SD-dSTORM signal from 286 CCPs from six cells. Ring diameters for FCHo2 (225 ± 12 nm) and AP2 (175 ± 17 nm) were significantly different (P = 0.00029, t test; n = 6). Scale bars, 100 nm. (F) Schematic representation of the domain structures of FCHo1, FCHo2, and the corresponding truncation or deletion mutants and chimeras used in this study. (G) Representative spinning disk confocal images of HeLa cells expressing the indicated FCHo1 and FCHo2 truncation or deletion mutants and chimeras tagged with the hemagglutinin (HA) epitope. Cells were fixed and colabeled with antibodies for the HA tag and endogenous AP2 α . Scale bar, 1 μm. wt, wild-type. (H) FCHo2 function in CME depends on its membrane-deforming FBAR domain and the ability of its APA domain to activate AP2. Normalized Tf-CME in control (shNS), clathrin (shCHC), or FCHo2-depleted HEK293T cells expressing the indicated FCHo2 deletion mutants or chimeras tagged with the HA epitope. Gray area indicates range between shFCHo2 and shFCHo2/rescue. Data are from n = 5 to 8 independent experiments as indicated at the bottom of each bar. Means ± S

Table 1. Antibodies used in this study. Used dilutions for immunofluorescence (IF) and Western blotting (WB) and clone or catalog number (clone/order) are provided. GAPDH, glyceraldehyde-3-phosphate dehydrogenase.

Antibody	Species	Clone/order	Source	Dilution IF	Dilution WB
FCHo2	Rabbit	A303-396A	Bethyl	-	1:200
FCHo2	Rabbit	RA130	H. McMahon	1:200	1:1000
FCHo1	Mouse	sc-105351	Santa Cruz	-	1:100
β-Actin	Mouse	ac-15	Sigma-Aldrich	-	1:10,000
Clathrin heavy chain	Rabbit	ab21679	Abcam	1:200	1:1000
Dynamin 1 + 2	Mouse	41	BD Biosciences	-	1:500
GAPDH	Rabbit			-	1:5000
GFP	Mouse	3E6	Invitrogen A-11120	1:200	
α-Tubulin	Mouse	DM1A	Sigma T9626		1:1000
Tf receptor	Mouse	Ab8598	Abcam	-	1:1000
Hip1R	Mouse	SAB1406767	Sigma	-	1:1000
AP2	Mouse	AP-6	Homebrew from hybridoma	1:100	1:1000
HA	Mouse	HA.11	Babco	1:200	1:1000
НА	Rat	9E7	Chromotek	1:1000	
Anti-rat AF647	Goat	712-605-153	Jackson Imm. Res.	1:200	
Anti-mouse AF568	Goat	A11031	Thermo	1:200	
Anti-mouse CF647	Goat	20281	Biotium	1:200	
Anti-rabbit CF680	Goat	20067	Biotium	1:200	

FCHo2 in the coupling of CCP growth and lifetime unraveled here. We tested these alternative models of FCHo2 action by analyzing the ability of short hairpin RNA (shRNA)-resistant chimeric or mutant versions of FCHo2 or FCHo1 (Fig. 3F) to rescue defective CME in cells depleted of endogenous FCHo2. Reexpression of wild-type (wt) FCHo2 fully rescued Tf-CME, whereas FCHo1 had no effect (Fig. 3H), consistent with the lack of effect of FCHo1 loss in control or FCHo2-depleted cells (Fig. 3, A to C). First, we analyzed FCHo2 truncation and deletion mutants lacking the F-BAR, APA, or μhomology domain (Fig. 3F) to rescue defective CME in cells lacking endogenous FCHo2. A truncation mutant harboring the F-BAR and APA domains but lacking the μ-homology domain fully restored Tf-CME to control levels, whereas a mutant lacking the F-BAR domain or lacking both the F-BAR and μ-homology domains was inactive and failed to correctly localize to CCPs (Fig. 3, G and H). Deletion of the APA domain, i.e., a mutant comprising the F-BAR and μ-homology domains, resulted in a dominant phenotype despite its accumulation at CCPs (Fig. 3, G and H). Hence, FCHo2 function in CME requires both a membrane-binding and membrane-deforming F-BAR domain and an AP2-activating APA domain that likely controls clathrin content. Our finding that FCHo2 assembles into ringlike structures at the rim of nascent CCPs (Fig. 3, D and E) together with the observed requirement for F-BAR domain function suggested that the specific physicochemical properties (i.e., shape, self-assembly, and charge distribution to enable specific binding to phosphatidylinositol 4,5-bisphosphate) of its F-BAR domain (20, 24) direct CCP growth and stability during the early stages of CCP assembly and invagination. To test this, we generated chimeric FCHo2 variants,

in which we replaced the F-BAR domain of FCHo2 with other F-BAR domains derived from FCHo1, FBP17 (formin-binding protein 17), or pacsin/syndapin 1, or, alternatively, with the more highly curved N-terminal helix-containing bin-amphiphysin-RVS (N-BAR) domain of endophilin A1 (2, 25). Notably, none of these chimeras were able to rescue defective Tf-CME in FCHo2-depleted cells; in fact, all of these chimeric proteins except for FCHo1 served as strong dominant-negative inhibitors of CME, although they were highly enriched at CCPs (Fig. 3, G and H). Last, site-specific mutations within the FCHo2-F-BAR domain that interfere either with dimerization (i.e., F38E/W73E) or with the recognition of the polar headgroup of phosphatidylinositol 4,5-bisphosphate (i.e., K146E/K165E) in the cytoplasmic leaflet of the plasma membrane (20) also abrogated FCHo2 function in CME (Fig. 3, G and H). Thus, FCHo2 controls CCP growth and stability via the specific membrane binding properties [i.e., direct association with phosphatidylinositol 4,5-bisphosphate, a crucial lipid for initiation of CME (2, 25)] and the shape of its F-BAR domain. Oligomerization of phosphatidylinositol 4,5-bisphosphate-bound F-BAR dimers likely directs the assembly of FCHo2 into a ring-like scaffold (Fig. 3, D and E) that may serve as a diffusion barrier (fig. S6) and/or promote clathrin assembly on the inside of the FCHo2 ring.

DISCUSSION

Our results unravel an unexpectedly close coupling between CCP growth and lifetime that controls the formation of productive CCPs and, thereby, CME in eukaryotic cells. The F-BAR domain protein FCHo2 controls this coupling via its (i) specific association with

Name	Backbone	Species and additional information	Primers or reference
psPAX2		Plasmid coding for lentiviral packaging GagPol	Addgene 12260 from Trono Lab
pMDG2		Plasmid coding for VSVG envelope	Addgene 12259 from Trono Lab
pGIPZ nonsilencing		Plasmid coding for lentiviral genome containing shRNA, IRES, and TurboGFP under hCMV promoter	Thermo Scientific Open Biosystems
pmRFP-CLC	mRFP-C1	mRFP-clathrin light chain	
peGFP-FCHo2	peGFP-C1	Mouse full-length FCHo2	A gift from H. McMahon, see (16)
pHA-C1	peGFP-C1 (Clontech)	Modified backbone with HA tag used for creating HA-labeled constructs	Age I–HA: CCGGTCGCCACCATGGCGTACCCATACGACGTCCCAGACTACGCGCT; HA–C1–Brs GI: TAGAGCGCGTAGTCTGGGACGTCGTATGGGTACGCCATGGTGGCGA
pHA-FCHo2 wt	pHA-C1	Mouse full-length FCHo2 with HA-tagged backbone	Cloned from peGFP-FCHo2 (16) using Age I/Bsr GI
pHA-FCHo1	pHA-C1	Full-length mouse FCHo1 in HA-tagged backbone	Cloned from FCHo1-pmCherryC1 (Addgene 27690)
pHA-FCHo2 F38E W73E	pHA-C1	Mouse FCHo2, dimerization defect	Cloned from peGFP-FCHo2 F38E W73E (16)
pHA-FCHo2 K146E K165E	pHA-C1	Mouse FCHo2, membrane binding mutant	Cloned from peGFP-FCHo2 K146E K165E (16)
pHA-FCHo2 FBAR-APA	pHA-C1	Mouse FCHo2 aa 1–394 (F-BAR domain and APA domain)	Forward: CATGGTCCTGCTGGAGTTCGTGAC; reverse: AATTCTCGAGTCAGTGTCTAGATACTGCTGGGG
pHA-FCHo2 APA μHD	pHA-C1	Mouse FCHo2 APA and μHD domains (306–873)	Forward: ATTTGTACAAGGAATGTCCTGACTTAGATTCG; reverse: rev_ eGFP_C
pHA FCHo2 APA	pHA-C1	Mouse FCHo2 aa 306–394 (APA domain)	Forward: ATTTGTACAAGGAATGTCCTGACTTAGATTCG; reverse: AATTCTCGAGTCAGTGTCTAGATACTGCTGGG
pHA FCHo2 ∆APA	pHA-C1	Mouse FCHo2 deletion of aa 306–394 (APA domain)	
pHA-FCHo2 FBAR FCHo1	pHA-C1	Chimera: mouse FCHo1 aa 1–353, mouse FCHo2 aa 356–873	Reverse: AATTGGTACCTTTTATTTAACTCATCGACTTTCTGC
pHA-FCHo2 FBAR FBP17	pHA-C1	Chimera: human FBP17 aa 1–368, mouse FCHo2 aa 356–873	Reverse: AATTGGTACCTTTTATTTAACTCATCGACTTTCTGC
pHA-FCHo2 FBAR Pacsin1	pHA-C1	Chimera: rat Pacsin1 aa 1–306 + 77 aa linker, mouse FCHo2 aa 356–873	Forward: AATTTGTACACAGATCTCGAGCTCAAGCTTGCCACC; reverse AATTGGTACCTCTTGGGGTTGGCGCCACC
pHA-FCHo2 FBAR Pacsin2	pHA-C1	Chimera: rat Pacsin2 aa 1–306 + 76 aa linker, mouse FCHo2 aa 356–873	Forward: AATTTGTACAaCGGACTCGGATCCGAATTCATGTC; reverse: AATTGGTACCTCTTAATGTCCTCCTTCACTG
pHA-FCHo2 NBAREndoA1-	pHA-C1	Chimera: rat endophilin A1 aa1–256, mouse FCHo2 aa356–873	Forward: AATTTGTACAGATCCATGTCGGTGGC; reverse: AATTGGTACCTCTGATATTCCCTTCTTGGTTG

plasma membrane phosphatidylinositol 4,5-bisphosphate, (ii) the assembly of its F-BAR domain into a ring-like scaffold at shallowly curved membranes (28) that outlines the perimeter of the assembling CCP (27), and (iii) the ability of its APA domain to trigger clathrin assembly and cargo recognition (21) by allosterically switching AP2 into its active conformation (23). In agreement with this model, FCHo2 has been shown to coassemble with AP2 and the early endocytic protein Eps15 into nanoclusters (21) at the edge of CCPs (27). By assembling into a membrane-associated ring-like scaffold, FCHo2 conceivably could act as a diffusion barrier for proteins and lipids (fig. S6) and/or direct the inward growth of the clathrin coat via local activation of AP2 (23) until the threshold for membrane invagination is reached. The latter is compatible with the observation

that in cell types forming stable flat hexagonal clathrin lattices (5, 6), these overgrow in the absence of FCHo2 (29), possibly due to a failure in directed clathrin growth to form nanoscale budding vesicles. Future studies will be needed to test this possibility. A kinetic coupling of early CCP growth to CCP lifetime and stability likely is a reflection of the metastable nature of the avidity-based endocytic protein network composed of multiple low-affinity interactions (4) that scale nonlinearly as the network expands in size (13). Similar rules may apply to the formation of other metastable structures in cells that need to be controlled in terms of size and stability to execute their function such as secretory transport vesicles (30, 31) and endocytic tubules (32, 33), budding viruses (34), signalosomes (35), or other types of signaling complexes.

MATERIALS AND METHODS

Computational model of CCPs

The model comprises three major early endocytic proteins:

- 1) Clathrin
- 2) AP2
- 3) FCHo2.

We modeled the membrane as a 36×36 hexagonal lattice, and proteins can bind at the vertices of the lattice. We assume the following interactions:

- 1) FCHo2 can bind to the membrane with an energy of ^EFCHo2.
- 2) Two FCHo2 proteins bound at neighboring sites interact with an energy ^EFCHo2-FCHo2.
- 3) If FCHo2 and AP2 are bound at the same site, they interact with an energy ^EFCHo2-AP2.
- 4) When FCHo2 interacts with AP2 (if they are bound at the same site), AP2 gets activated. AP2 stays activated as long as it is bound to the membrane, even if FCHo2 unbinds.
- 5) Nonactivated AP2 binds to the membrane with a low-energy ${}^{E}AP2$, while the activated AP2 binds to the membrane more strongly (36), with an energy ${}^{E}AP2$ -act such that $|{}^{E}AP2| << |EAP2$ -act | (see values of the parameters in table S1).
- 6) Clathrin can bind to the membrane only if AP2 is already present at the same site. Clathrin and AP2 interact with an energy ^EAP2-cl.
- 7) If two clathrin proteins are bound at neighboring sites, then they interact with an energy $^{E}cl-cl$.

All values of the parameters used in the model are reported in table S1. Each FCHo2 unit binding to the membrane in the model is considered to be a dimer, as FCHo2 forms stable dimers (24). We allowed both FCHo2 and clathrin to form higher-order structures by associating an attractive pairwise interaction between any pair of neighboring FCHo2 dimers or any pair of neighboring clathrin molecules. To account for the tendency of clathrin to form higher-order structures, stronger attractive energy between pairs of neighboring clathrin molecule was used in the model (see table S1).

The number of AP2 and clathrin proteins present in the simulations was fixed to a number of 180 each. Different simulations were performed with a different number of FCHo2 proteins available, from 5 to 50, to investigate the effect of FCHo2 on the formation of clathrin clusters. The simulations were performed as follows. At each time step, for each of the endocytic proteins, one of the proteins in the pool is selected at random. If the selected protein is unbound, then a site on the lattice is selected at random. If the site is already occupied by a protein of the same kind, then nothing happens. If no protein of the same species is bound at the selected site, then the selected protein binds to the membrane at that site. However, as discussed above, clathrin can bind only if AP2 is present. If the selected protein is already bound, then it can unbind with a probability $\exp(E_{tot})$, where E_{tot} is the total energy of the bound protein, taking into account all the contributions from the interactions listed above (all interactions are considered additive). Simulations were performed for a total of 10⁸ steps, and snapshots were recorded every 1000 steps. A total of 100 simulations were performed for each of the different choices for the number of FCHo2 proteins. In each simulation, the formation of clathrin clusters as a function of time was monitored as follows. In each snapshot, clusters were detected by considering the connectivity of clathrin interactions on the lattice. The trajectories of the center of mass of each cluster consisting of more than 10 clathrin proteins and lasting more than 5×10^6 steps

were recorded, and the size of the cluster as a function of time was monitored.

Plasmids and cloning

The plasmids and polymerase chain reaction (PCR) primers used in this study are listed above. Mutations in pHA (plasmid hemagglutinin tag)–FCHo2 were introduced using Phusion mutagenesis (Thermo). Deletion and chimeric constructs were produced by standard PCR cloning techniques. All plasmids were verified by double-stranded DNA sequencing (Table 2).

Cell lines

Cos7, BSC1, HeLa, and HEK293T cells were from the American Type Culture Collection (ATCC). All cells were cultured in Dulbecco's modified Eagle's medium [glucose (4.5 g/liter), with L-glutamine, without sodium pyruvate] supplemented with 10% (v/v) fetal bovine serum and penicillin (100 U/ml) at 37°C and 5% CO₂. Cell lines were not used beyond passage 30 from original and routinely tested for mycoplasma contaminations on a monthly basis.

Lentivirus production and transduction

shRNA-expressing lentiviruses were produced from HEK293T after calcium phosphate transfection of psPAX2, pMDG2, and pGIPZ (OpenBiosystem, Thermo Fisher). pGIPZ human clathrin (V3LHS_350703, 5'-ACGTGTTATGGAGTATATT-3'), pGIPZ human FCHo2 (V3LHS_350712, 5'-AGCATTTGACAAGGATCCT-3'), and pGIPZ human FCHo1 (V2LHS_255856, 5'-TAAATTCCTCATG-CACCTG-3') were used to knock down the indicated proteins. pGIPZ nonsilencing shRNA construct (shNS, no. RHS4346) was used as a negative control. Two to 3 days after transfection, viral supernatants were harvested, cleared by centrifugation (5 min, 1500g), and filtered through a 0.45-µm filter. Viral supernatants were directly used for three rounds of infection of Cos, HeLa, and HEK cells at days 1 and 2, followed by 3 days of selection in puromycin to eliminate nontransduced cells. On day 5 after the first transduction, cells were reseeded for transfection, uptake, or either directly fixed for EM analysis or lysed for Western blot analysis.

Plasmid transfections

For transient overexpression of proteins in HeLa or Cos7 knockdown cells, plasmids were transfected using Lipofectamine 2000 (Life Technologies) according to the manufacturer's protocol. Transfection of lentiviral transduced HEK293T cells for rescue experiments was performed using calcium phosphate.

TIRF microscopy

Transfected HeLa and Cos7 cells were seeded on Matrigel-coated coverslips. TIRF was performed using a Nikon Eclipse Ti microscope, equipped with an incubation chamber (Okolab), a $60\times$ TIRF objective [Apo TIRF 1.49 numerical aperture (NA), Nikon], a sCMOS camera (Neo, Andor), a 200-W mercury lamp (Lumen 200, Prior), four laser lines (405, 488, 568, and 647 nm from Omicron), an appropriate dichroic mirror (Di01-R405/488/561/635), and emission filter (FF01-446/523/600/677) and operated by the open-source ImageJ-based micromanager software. Imaging was performed at 37°C in live cell imaging buffer (Hanks' balanced salt solution $+Ca^{2+} + Mg^{2+}$, 5% fetal calf serum) over 180 s at an imaging rate of 0.5 Hz with a final pixel size of 108 nm. For all time-lapse movies of dual-transfected cells, the 488-nm channel was acquired before the 568-nm channel.

Image analysis for TIRF imaging

Quantitative CCP analysis followed the general methodological framework first published in (12, 37) and used the associated cmeAnalysis MATLAB package that was subsequently published in (7). Here, we used a customized adaptation of the main features of the cmeAnalysis MATLAB package together with some newly written analysis functions. First, CCPs were detected independently in individual frames and then tracked and gap closed, both using the functionality from the cmeAnalysis package. We customized our tracking parameters through validation of the tracking results on experimental data to ensure that the trajectories of long-lived, low-motility structures with fluctuating intensities are not excessively broken up into smaller segments.

Because the focus of this study was to study the dynamics of the productive population (as opposed to maturation events related to the transition between abortive and productive populations), we adapted the CCP selection criteria to constrain our analyses to the population of CCPs that are most likely true internalizations, using selection criteria based on recent findings from (7, 11). For this purpose, we constrained the resultant trajectories to those CCPs with low lateral mobility (average frame-to-frame displacement) and intermediate-to-high lifetimes [see (11)]. Specifically, on the basis of the distribution of the motilities of the subset of extremely long-lived CCPs (>120 s), which—pooled across all available movies peaks between 0.6 and 0.9 pixel per frame, we chose an upper threshold of 1.8 pixel per frame for the permissible motility and further constrained the lifetimes to the range above 20 s (see fig. S1), thus excluding the large pool of short-lived (and often highly motile) CCSs of unclear origin. Thus, in the following, when we refer to a "CCP" in the context of the analysis, this always represents a CCS trajectory that meets these constraint criteria (unless otherwise stated). Intensity and lifetime analysis were performed after this constraint step using the methods described in (7, 12, 37), including the readout of CCP intensities above background for five frames before the first and five frames after the last detected time point.

Lifetime analysis

The initiation density (compare Fig. 2) was calculated, as previously described, by counting the number of uncensored trajectories of the relevant lifetime range that are observed during the entire movie, dividing by the total cell area, and correcting for the higher censoring probability of longer trajectories (which is physically equivalent to dividing this CCP density by the length of the available time window during which CCPs of this lifetime can be initiated without being censored by the end of the movie). The resulting initiation density is thus in dimensions of [# of CCPs/(area*time)] and units of [# of CCPs/(micron²*second)] and represents the number of CCPs of a given lifetime that are initiated per time per area. For better visibility of differences of the time dynamics in the lifetime distribution, we show the cumulative instead of the raw function. The time constant was determined through a single exponential fit of the lifetime distribution in the range between 20 and 120 s. The single exponential was chosen to yield a robust first-order quantitative descriptor of the maturation dynamics of the productive population of CCPs (consistent with fitting approaches of previous studies); the fitting range was limited to two-thirds of the shortest movie length to limit the influence of noise (since, in this system, the longest-lived CCPs inherently have the lowest absolute numbers of uncensored trajectories available). The total absolute initiation density represents the total

number of CCP initiations (of the specified lifetime and mobility constraints) that are initiated per area per time across all lifetimes up to the value (movie length, 10) and irrespective of censoring status (i.e., including both uncensored and right-censored trajectories).

Intensity analysis

For the maximum intensities (see Fig. 2), we first calculated the lifetime intensity "cohorts," i.e., the intensity time profiles averaged over all CCPs of the specified lifetime [as described in (37), but with the intensity traces smoothed by applying a Gaussian filter to the intensity traces both into the dimension of elapsed time of the trajectory and into the dimension of the included lifetimes, with a filter size of 3.5 frames], where intensities were normalized to a 5 to 95% scale (such that an object whose brightness corresponds to the threshold of the dimmest 5% of total objects has normalized intensity 0, and an object whose brightness corresponds to the threshold of the brightest 5% of total objects has normalized intensity 100); we then determined the peak normalized intensity of the relevant cohort above background for the individual movie and then averaged these intensities across all available movies. The intensity profiles were calculated analogously for dual-channel data. The lag times (between the individual color channels) for the recruitment and departure phases were measured by subtracting the time points at which the respective traces reached 50% of the maximal intensity above background of the respective lifetime cohort. For the plot of maximal intensities of the dual-channel movies, the intensities were first normalized within each individual movie, after which the maximum intensity values of the individual cohorts were averaged over all available movies, but here, the normalization was such that the average intensity of the 60-s cohort was set to 1 for better visualization of the differences between the color channels.

Immunocytochemistry

Nontransfected or transfected HeLa cells on coverslips were fixed for 5 min with methanol at -20°C , washed two times with phosphate-buffered saline (PBS), incubated in blocking solution [30% goat serum, 20 mM Na₂HPO₄ (pH 7.4), 0.3% Triton X-100, and 100 mM sodium chloride] for 30 min, and incubated with primary antibodies diluted in blocking solution for 1 hour. After three washes with PBS, secondary antibodies diluted in blocking solution were incubated for 1 hour, followed by three washes in PBS. Protein stains were analyzed either by dSTORM (see below) or Spinning Disk Confocal Microscopy (Nikon, Andor) after staining nuclei with Hoechst 33258 (1 μ g/ml; Thermo) and mounting in Immomount (Thermo).

Sample preparation for dSTORM imaging

For dSTORM imaging, HeLa cells were grown on acid-cleaned coverslips (170 \pm 5 μm ; Carl Roth GmbH) and fixed in methanol at $-20^{\circ}C$ for 5 min. After fixation, cells were washed three times with PBS at room temperature. Immunocytochemistry was performed as described above, except the secondary antibodies conjugated to CF647 or CF680 (Biotium) were used at 10 $\mu g/ml$. Fluorescent beads (40 nm dark Red, Life Technologies) were diluted in poly-L-lysine (PLL) and bound to the coverslips for 5 min at room temperature. Samples were washed three times in PBS and mounted in imaging buffer [50 mM Tris-HCl and 10 mM NaCl (pH 8)] with 10 mM β -mercaptoethylamine (Sigma 30070) and an oxygen scavenging system consisting of glucose oxidase (0.5 mg/ml; Sigma G2133), catalase (40 $\mu g/ml$; Sigma C100), and 10% (w/v) glucose. Stained samples were mounted on slides providing a

100-µl spherical void (Carl Roth, H884.1) with imaging buffers, sealed with picodent twinsil, and imaged within 8 hours.

Dual-color dSTORM imaging and analysis

The custom-built SD-dSTORM system based on a custom laser combiner and TIRF illuminator system, a Nikon Eclipse Ti research microscope, an emission splitter (OptoSplit II, Cairn Optics), and an EMCCD (512 × 512; DU-897E, Andor Instruments) controlled by µManager was previously described (38). For activation and excitation, we used laser lines at 405 nm (50 mW; Qioptiq) and 643 nm (150 mW; Toptica), respectively. Sample illumination occurred in wide-field mode with excitation intensities of 0.36 kW/cm² at 643 nm. The laser beams were reflected off a quadband dichroic mirror (Di01-R405/488/561/635). We collected the emission of dyes excited with 643 nm using a longpass filter (BLP01-635R). All filters were from AHF Analysentechnik. The combination of a 100× 1.49 NA objective and a 1.5× Optovar and the EMCCD with a pixel size of $16 \times 16 \,\mu\text{m}^2$ resulted in pixel sizes of $105 \times 105 \,\text{nm}^2$ in the image. Initially, the fluorescent dyes were switched off until single molecule blinking was detected. Image acquisition was performed at a frame rate of 33 Hz, typically for 20,000 frames. Lower labeling density was compensated by reactivation of CF647 with low intensities of ultraviolet light (405 nm, 0.05 W/cm²). Single molecules were localized with the open-source software rapidSTORM 3.2 (39). RapidSTORM performs a Gaussian fit (Levenberg-Marquardt parameter estimation) to each single-molecule signal using a fixed PSF-FWHM (point spread function's full width at half maximum) of 300 nm for CF647. The fitting window radius was set to 600 nm and the minimum spot distance to five pixels. The minimum threshold of signal intensity (i.e., the total intensity under the 2D Gaussian fit) was set to 1000 ADC (analog per digital counts). The "two-kernel improvement" was used to prevent the detection of multiple singlemolecule localizations appearing in the same frame within a radius of 600 nm. The rapidSTORM output is a list of x, y, and z coordinates with subpixel localization accuracy, the total intensities (integrated Gaussian fit), and the frame number of each detected single molecule. Drift correction was performed by a custom-written program based on Python 2.7 that uses fluorescent beads as fiduciary markers. The accuracy of this correction was calculated from the SD σ of the distances of the corrected bead localizations as 2.35 o. Typically, we achieved a drift correction accuracy of 4 to 5 nm. The final dSTORM image of CF647/CF680-labeled structures had an image resolution of 20 to 30 nm and was reconstructed using a 10-nm pixel size.

Superimposition and analysis of single-molecule localization data

The CCPs for averaging were selected on the basis of the presence of AP2 in the dSTORM image using a custom ImageJ script that created regions of interest with the center at the position of the mouse click. Particle averaging was performed using a custom program written in Python, selecting the corresponding localization data from the rapidSTORM list of all localizations within a 400×400 –nm² window. The superimposed localizations from all selections were plotted together using rapidSTORM with a pixel size of 10 nm. Radial distance measurements were performed on averaged dual-color SD-dSTORM images. Python scripts for drift correction, grouping, center averaging, and distance measurements of dSTORM images can be provided upon request.

Immunoblot analysis

Knockdown of FCHo1, FCHo2, and clathrin heavy chain (CHC) was routinely verified by immunoblot analysis. Cells were harvested 5 days after transduction with shRNA-expressing lentiviruses in lysis buffer [20 mM Hepes (pH 7.4), 100 mM KCl, 2 mM MgCl₂, 1 mM phenylmethylsulfonyl fluoride, 0.1% protease inhibitor cocktail, and 1% Triton X-100] and incubated on ice for 30 min, followed by centrifugation at 17,000g for 20 min at 4°C. Protein concentrations were determined via Bradford assay, and 10 to 15 μg of protein was loaded onto a 4 to 15% acrylamide gel (Bio-Rad) for SDS–polyacrylamide gel electrophoresis, followed by immunoblotting. Immunoblot development was performed using ECL (enhanced chemiluminescence) and the LI-COR Odyssey Fc imager.

Tf uptake and surface labeling

Lentivirally transduced HeLa, Cos7, or HEK293T cells were seeded on Matrigel- or PLL-coated glass coverslips. Cells were serum starved for 1 hour and used for Tf uptake and subsequent surface labeling. For quantitative Tf uptake, cells were treated with Tf–Alexa 568 or Tf–Alexa 647 (25 $\mu g/ml$; Life Technologies) for 10 min at 37°C. After being washed twice with ice-cold PBS, cells were acid washed at pH 5.5 (0.1 M sodium acetate and 0.2 M NaCl) for 1 min on ice to remove surface-bound Tf, followed by two times of washing with ice-cold PBS. Cells were subsequently fixed with 4% paraformaldehyde (PFA) for 45 min at room temperature, stained with Hoechst, and mounted in Immomount.

Tf uptake for different cell lines was analyzed using an Epifluorescence microscope (Nikon Eclipse Ti microscope) equipped with optimal filters (eGFP filter set: F36-526; TexasRed filter set: F36-504; Cy5 filter set: F46-009; DAPI filter set: F46-000, AHF Analysentechnik), a 20× objective (Nikon), a sCMOS camera (Neo, Andor), and a 200-W mercury lamp (Lumen 200, Prior) and operated by the open-source ImageJ-based micromanager software. Internalized and surface-bound Tf was quantified in randomly selected eGFP-positive cells and normalized to the cell area using automated software (ImageJ).

For knockdown-rescue Tf uptake experiments, HEK293T cells were seeded in PLL-coated 96-well plates (Corning). Transfections of hemagglutinin (HA)-tagged constructs were performed in triplicates. Tf uptakes with Tf Alexa 647 were performed as described above. PFA-fixed cells were stained for HA-tagged proteins using anti-HA (mouse, Babco) and Alexa 568 secondary antibodies and for nuclei using Hoechst 33258 as described above. Plates were imaged with a 20× air objective in an ArrayScan automated microscope (Thermo Scientific) operated with Cellomics software. Cellular nuclei were automatically focused based on maximal fluorescence signal in Hoechst channel. Quantitative image analysis was performed using Cellomics Cell Viewer. Briefly, total punctuate Tf signal with a minimal size was quantified within TurboGFP and HA doublepositive masks and normalized for mask area. All quantitative uptake data were normalized to shFCHo2-transduced cells transfected with the wt HA-FCHo2 construct.

Electron microscopy

Lentiviral knockdowns for shNS and shFCHo2 were performed as described in Cos7 cells (Fig. 2, I and K, and fig. S4) and HEK293T cells (Fig. 2, I and J) grown in 6-cm plastic dishes. Distinct morphological intermediates (Fig. 2J) were analyzed in HEK293T cells in which shallow intermediates can be detected more reliably compared

with Cos7 cells due to differences in cell shape. Cells were fixed with 2% glutaraldehyde in PBS. After rinsing in fresh PBS, cells were mechanically detached by scratching, pelleted, and embedded into gelatin. Following osmification with aqueous 1% osmium tetroxide, samples were stained en bloc with 1% aqueous uranyl acetate and embedded in epoxy resin. Sections were viewed with a Zeiss 910 transmission electron microscope, and micrographs were taken along the cell perimeter at ×20,000. For morphometric analysis, images were combined to reconstruct the perimeter of a cell, and the number of clathrin-coated shallow, U-shaped, constricted, or completely assembled (i.e., CCVs) intermediates at a distance within 1 µm from the plasma membrane was counted. The outline of the plasma membrane for individual profiles from each intermediate was traced, centered, and rotated using ImageJ. The depth of the membrane for each profile was measured as the maximum profile distance from the plasma membrane for shallow, U-shaped, and constricted CCPs or the vesicle diameter for CCVs.

Statistical analysis

For analysis of experiments comprising multiple independent experiments (n), statistically significant estimates for each sample were obtained by choosing an appropriate sample size, correlating to 15 to 30 images per condition for microscopy-based quantifications. Cells were chosen arbitrarily according to the fluorescent signal in a separate channel, which was not used for quantification. All statistical tests were performed using the two-tailed, paired or unpaired t test, or one-sample t test using Prism software.

SUPPLEMENTARY MATERIALS

Supplementary material for this article is available at http://advances.sciencemag.org/cgi/content/full/5/11/eaax5775/DC1

- Fig. S1. Automatic detection, filtering, and quantification of CCP dynamics from TIRF movies. Fig. S2. FCHo2 arrives as early as clathrin is linearly recruited and leaves CCPs before scission.
- Fig. S3. Impaired Tf-CME in FCHo2-depleted HEK293T and HeLa cells.
- Fig. S4. EM analysis of clathrin-coated endocytic structures following lentiviral knockdown of FCHo2 protein expression.
- Fig.~S5.~Expression~of~HA-tagged~FCHo2~mutants,~deletions,~and~chimeras.
- Fig. S6. Limited diffusion of plasma membrane Harvey rat sarcoma viral oncogene homolog (hRas)–SNAP into the center of CCPs delineated by eGFP-FCHo2.
- Table S1. Interaction energies between the different proteins and the proteins and the membrane, in units of $k_{\rm B}T$.

View/request a protocol for this paper from Bio-protocol.

REFERENCES AND NOTES

- F. M. Brodsky, Diversity of clathrin function: New tricks for an old protein. Annu. Rev. Cell Dev. Biol. 28. 309–336 (2012).
- M. Kaksonen, A. Roux, Mechanisms of clathrin-mediated endocytosis. Nat. Rev. Mol. Cell Biol. 19, 313–326 (2018).
- 3. M. S. Robinson, Forty years of clathrin-coated vesicles. *Traffic* 16, 1210–1238 (2015).
- E. M. Schmid, H. T. McMahon, Integrating molecular and network biology to decode endocytosis. *Nature* 448, 883–888 (2007).
- J. Grove, D. J. Metcalf, A. E. Knight, S. T. Wavre-Shapton, T. Sun, E. D. Protonotarios, L. D. Griffin, J. Lippincott-Schwartz, M. Marsh, Flat clathrin lattices: Stable features of the plasma membrane. *Mol. Biol. Cell* 25, 3581–3594 (2014).
- M. Lampe, S. Vassilopoulos, C. Merrifield, Clathrin coated pits, plaques and adhesion. J. Struct. Biol. 196, 48–56 (2016).
- F. Aguet, C. N. Antonescu, M. Mettlen, S. L. Schmid, G. Danuser, Advances in analysis
 of low signal-to-noise images link dynamin and AP2 to the functions of an endocytic
 checkpoint. *Dev. Cell* 26, 279–291 (2013).
- E. Cocucci, F. Aguet, S. Boulant, T. Kirchhausen, The first five seconds in the life of a clathrin-coated pit. Cell 150, 495–507 (2012).
- D. Dambournet, K. A. Sochacki, A. T. Cheng, M. Akamatsu, J. W. Taraska, D. Hockemeyer,
 D. G. Drubin, Genome-edited human stem cells expressing fluorescently labeled

- endocytic markers allow quantitative analysis of clathrin-mediated endocytosis during differentiation. *J. Cell Biol.* **217**, 3301–3311 (2018).
- J. B. Doyon, B. Zeitler, J. Cheng, A. T. Cheng, J. M. Cherone, Y. Santiago, A. H. Lee, T. D. Vo, Y. Doyon, J. C. Miller, D. E. Paschon, L. Zhang, E. J. Rebar, P. D. Gregory, F. D. Urnov, D. G. Drubin, Rapid and efficient clathrin-mediated endocytosis revealed in genomeedited mammalian cells. *Nat. Cell Biol.* 13, 331–337 (2011).
- S. H. Hong, C. L. Cortesio, D. G. Drubin, Machine-learning-based analysis in genomeedited cells reveals the efficiency of clathrin-mediated endocytosis. *Cell Rep.* 12, 2121–2130 (2015).
- D. Loerke, M. Mettlen, D. Yarar, K. Jaqaman, H. Jaqaman, G. Danuser, S. L. Schmid, Cargo and dynamin regulate clathrin-coated pit maturation. *PLOS Biol.* 7, e57 (2009).
- Y. Li, Y. Wang, G. Huang, J. Gao, Cooperativity principles in self-assembled nanomedicine. Chem. Rev. 118, 5359–5391 (2018).
- O. Avinoam, M. Schorb, C. J. Beese, J. A. Briggs, M. Kaksonen, ENDOCYTOSIS. Endocytic sites mature by continuous bending and remodeling of the clathrin coat. Science 348, 1369–1372 (2015).
- D. Bucher, F. Frey, K. A. Sochacki, S. Kummer, J.-P. Bergeest, W. J. Godinez, H.-G. Kräusslich, K. Rohr, J. W. Taraska, U. S. Schwarz, S. Boulant, Clathrin-adaptor ratio and membrane tension regulate the flat-to-curved transition of the clathrin coat during endocytosis. *Nat. Commun.* 9, 1109 (2018).
- B. L. Scott, K. A. Sochacki, S. T. Low-Nam, E. M. Bailey, Q. Luu, A. Hor, A. M. Dickey,
 S. Smith, J. G. Kerkvliet, J. W. Taraska, A. D. Hoppe, Membrane bending occurs at all stages of clathrin-coat assembly and defines endocytic dynamics. *Nat. Commun.* 9, 419 (2018).
- K. A. Sochacki, J. W. Taraska, From flat to curved clathrin: Controlling a plastic ratchet. Trends Cell Biol. 29, 241–256 (2018).
- A. Frost, V. M. Unger, P. De Camilli, The BAR domain superfamily: Membrane-molding macromolecules. Cell 137, 191–196 (2009).
- B. J. Peter, H. M. Kent, I. G. Mills, Y. Vallis, P. J. Butler, P. R. Evans, H. McMahon, BAR domains as sensors of membrane curvature: The amphiphysin BAR structure. Science 303, 495–499 (2004).
- W. M. Henne, E. Boucrot, M. Meinecke, E. Evergren, Y. Vallis, R. Mittal, H. T. McMahon, FCHo proteins are nucleators of clathrin-mediated endocytosis. *Science* 328, 1281–1284 (2010).
- L. Ma, P. K. Umasankar, A. G. Wrobel, A. Lymar, A. J. McCoy, S. S. Holkar, A. Jha, T. Pradhan-Sundd, S. C. Watkins, D. J. Owen, L. M. Traub, Transient Fcho1/2-Eps15/R-AP-2 nanoclusters prime the AP-2 clathrin adaptor for cargo binding. *Dev. Cell* 37, 428–443 (2016)
- P. K. Umasankar, L. Ma, J. R. Thieman, A. Jha, B. Doray, S. C. Watkins, L. M. Traub, A clathrin coat assembly role for the muniscin protein central linker revealed by TALEN-mediated gene editing. *eLife* 3, e04137 (2014).
- G. Hollopeter, J. J. Lange, Y. Zhang, T. N. Vu, M. Gu, M. Ailion, E. J. Lambie, B. D. Slaughter, J. R. Unruh, L. Florens, E. M. Jorgensen, The membrane-associated proteins FCHo and SGIP are allosteric activators of the AP2 clathrin adaptor complex. *eLife* 3, e03648 (2014).
- W. M. Henne, H. M. Kent, M. G. J. Ford, B. G. Hegde, O. Daumke, P. J. G. Butler, R. Mittal, R. Langen, P. R. Evans, H. T. McMahon, Structure and analysis of FCHo2 F-BAR domain: A dimerizing and membrane recruitment module that effects membrane curvature. Structure 15, 839–852 (2007).
- V. Haucke, M. M. Kozlov, Membrane remodeling in clathrin-mediated endocytosis. J. Cell Sci. 131, jcs216812 (2018).
- H. T. McMahon, E. Boucrot, Molecular mechanism and physiological functions of clathrin-mediated endocytosis. Nat. Rev. Mol. Cell Biol. 12, 517–533 (2011).
- K. A. Sochacki, A. M. Dickey, M.-P. Strub, J. W. Taraska, Endocytic proteins are partitioned at the edge of the clathrin lattice in mammalian cells. *Nat. Cell Biol.* 19, 352–361 (2017).
- W. Zhao, L. Hanson, H.-Y. Lou, M. Akamatsu, P. D. Chowdary, F. Santoro, J. R. Marks, A. Grassart, D. G. Drubin, Y. Cui, B. Cui, Nanoscale manipulation of membrane curvature for probing endocytosis in live cells. *Nat. Nanotechnol.* 12, 750–756 (2017).
- E. E. Mulkearns, J. A. Cooper, FCH domain only-2 organizes clathrin-coated structures and interacts with Disabled-2 for low-density lipoprotein receptor endocytosis. *Mol. Biol. Cell* 23, 1330–1342 (2012).
- B. Antonny, J. Audhya, M. Bagnat, J. von Blume, J. A. Briggs, C. Giraudo, P. S. Kaeser,
 E. Miller, K. Reinisch, I. F. Sbalzarini, M. Schuldiner, J. Shen, S. Takamori, P. Verstreken,
 T. Walther, Directing traffic into the future. *Dev. Cell* 27, 480–484 (2013).
- J. S. Bonifacino, B. S. Glick, The mechanisms of vesicle budding and fusion. Cell 116, 153–166 (2004).
- E. Boucrot, A. P. A. Ferreira, L. Almeida-Souza, S. Debard, Y. Vallis, G. Howard, L. Bertot,
 N. Sauvonnet, H. T. McMahon, Endophilin marks and controls a clathrin-independent endocytic pathway. *Nature* 517, 460–465 (2015).
- H.-F. Renard, M. Simunovic, J. Lemière, E. Boucrot, M. D. Garcia-Castillo, S. Arumugam,
 V. Chambon, C. Lamaze, C. Wunder, A. K. Kenworthy, A. A. Schmidt, H. T. McMahon,

SCIENCE ADVANCES | RESEARCH ARTICLE

- C. Sykes, P. Bassereau, L. Johannes, Endophillin-A2 functions in membrane scission in clathrin-independent endocytosis. *Nature* **517**, 493–496 (2015).
- W. I. Sundquist, H.-G. Kräusslich, HIV-1 assembly, budding, and maturation. Cold Spring Harb. Perspect. Med. 2, a006924 (2012).
- G. A. Cope, R. J. Deshaies, COP9 signalosome: A multifunctional regulator of SCF and other cullin-based ubiquitin ligases. Cell 114, 663–671 (2003).
- S. Höning, D. Ricotta, M. Krauss, K. Späte, B. Spolaore, A. Motley, M. Robinson, C. Robinson, V. Haucke, D. J. Owen, Phosphatidylinositol-(4,5)-bisphosphate regulates sorting signal recognition by the clathrin-associated adaptor complex AP2. Mol. Cell 18, 519–531 (2005).
- D. Loerke, M. Mettlen, S. L. Schmid, G. Danuser, Measuring the hierarchy of molecular events during clathrin-mediated endocytosis. *Traffic* 12, 815–825 (2011).
- A. Lampe, V. Haucke, S. J. Sigrist, M. Heilemann, J. Schmoranzer, Multi-colour direct STORM with red emitting carbocyanines. *Biol. Cell* 104, 229–237 (2012).
- S. Wolter, A. Löschberger, T. Holm, S. Aufmkolk, M.-C. Dabauvalle, S. van de Linde, M. Sauer, rapidSTORM: Accurate, fast open-source software for localization microscopy. Nat. Methods 9, 1040–1041 (2012).

Acknowledgments: We thank M. Ringling and D. Löwe for technical assistance. **Funding:** Supported by grants from the German Research Foundation to V.H. (SFB958/A07 and TRR186/A08), F.N. (SFB958/A04 and TRR186/A12), and J.S. (SFB958/Z02); the European Research Council to F.N. (ERC CoG grant 772230); the National Science Foundation to C.C. (CHE-1265929,

CHE-1738990, and PHY-1427654); the Welch Foundation to C.C. (C-1570); and the Einstein Foundation Berlin (Einstein Visiting Fellowship to C.C.). Simulations were performed on the computer clusters of the Center for Research Computing at Rice University, supported, in part, by the Big-Data Private-Cloud Research Cyberinfrastructure MRI award (NSF grant CNS-1338099), and on the clusters of the Department of Mathematics and Computer Science at Freie Universität, Berlin. Author contributions: V.H. and M.L. supervised the study, conceived the research and wrote the manuscript. M.L. and I.L. carried out the EM analyses and all biochemical and molecular biological experiments; M.L. performed Tf uptake studies and analyzed CCP dynamics together with D.L. Super-resolution microscopy was performed by M.L. aided by J.S. C.C. and F.N. did all the computational simulations. Competing interests: The authors declare that they have no competing interests. Data and materials availability: All data needed to evaluate the conclusions in the paper are present in the paper and/or the Supplementary Materials. Additional data related to this paper may be requested from the authors.

Submitted 4 April 2019 Accepted 25 September 2019 Published 27 November 2019 10.1126/sciadv.aax5775

Citation: M. Lehmann, I. Lukonin, F. Noé, J. Schmoranzer, C. Clementi, D. Loerke, V. Haucke, Nanoscale coupling of endocytic pit growth and stability. Sci. Adv. 5, eaax5775 (2019).



Nanoscale coupling of endocytic pit growth and stability

Martin Lehmann, Ilya Lukonin, Frank Noé, Jan Schmoranzer, Cecilia Clementi, Dinah Loerke and Volker Haucke

Sci Adv 5 (11), eaax5775. DOI: 10.1126/sciadv.aax5775

ARTICLE TOOLS http://advances.sciencemag.org/content/5/11/eaax5775

SUPPLEMENTARY http://advances.sciencemag.org/content/suppl/2019/11/21/5.11.eaax5775.DC1

REFERENCES This article cites 39 articles, 8 of which you can access for free

http://advances.sciencemag.org/content/5/11/eaax5775#BIBL

PERMISSIONS http://www.sciencemag.org/help/reprints-and-permissions

Use of this article is subject to the Terms of Service